

# Information systems modeling

UDC 621.396.962

doi: <https://doi.org/10.20998/2522-9052.2025.1.04>Viktor Kudriashov<sup>1</sup>, Oleksii Kolomiitsev<sup>2</sup>, Kostyantyn Lukin<sup>1</sup>, Mykola Slipchenko<sup>2</sup>, Paweł Bernat<sup>3</sup><sup>1</sup> O.Ya. Usikov Institute for Radiophysics and Electronics, Kharkiv, Ukraine<sup>2</sup> National Technical University “Kharkiv Polytechnic Institute”, Kharkiv, Ukraine<sup>3</sup> Polish Air Force University, Deblin, Poland

## METHODOLOGY OF THE NUMERICAL MODELLING OF PARAMETERS DETERMINATION OF THE RADIOMETRIC IMAGE OF REMOTE EARTH SURFACE SENSING BY BISTATIC RADIOMETER

**Abstract.** The on-board bistatic radiometer (BR) provides sufficiently high-quality mapping of various terrestrial surfaces. **The subject of study** in the article is the determination of parameters of radiometric images (RI) of earth surfaces based on the BR construction options that are technically feasible. **The aim of the research** is to develop a methodology for numerical modelling of RI parameters calculation during remote sensing of the earth's surfaces by BR. **Tasks:** To consider the range of the radar, accounting for image bands, detection, and measurement of course difference, and resolution along the carrier's flight path and across its path. The task also includes the calculation of the difference Doppler frequency correction (DDFC) of payload signals, root mean square deviations (RMSD) of pitch difference errors and DDFC errors. **Methods** used: analysis and synthesis of the obtained output RI parameters according to possible construction options. The following **results** were obtained. A methodology for numerical modelling of RI parameters determination during remote sensing of a low-contrast payload such as grass-concrete is developed. The AN-14 ‘Bee’ aircraft was chosen as a carrier for the BR, and the 22 GHz bandwidth of the sub-waveband was chosen for the BR 3 mm. The analysis was carried out for six possible variants of the mapping system. The ranges of the systems, the values of image bands, and the DDFC of objects are calculated, considering the accepted technical characteristics of the radar and the influence of the atmosphere. The RI characteristics at a probability of correct detection of 0.5 are presented. The image parameters for measuring the differences in the stroke and DDFC of mapping objects are given. The number of pixels (pitch differences) in the image row, the resolution along the carrier path, across the path, and at the DDFC were calculated. The number of Doppler filters for each pitch difference, the RMSD of the pitch difference measurement, and the RMSD of the object's DDFC measurement were obtained. The values of the fluctuation sensitivity of the BR were calculated for the following design variants. **Conclusions.** Based on the results of numerical modelling, the analysis of the information capacity per RI during remote sensing of earth surfaces by an onboard system that is spaced apart is carried out. A promising area for further research may be the introduction of a very weak broadband noise sensing signal into the mapping system and the assessment of the impact of interference that is spatially correlated in the BR.

**Keywords:** numerical modelling methodology; radiometric image; remote sensing; bistatic radiometer; range; image band; Doppler frequency correction; resolution.

### Introduction

**Problem definition.** The resolution of images in well-known radiometric mapping systems is determined only by the radiation pattern (RP) of the antennas and the fluctuation sensitivity of the radiometer [1, 2]. This minimal set of parameters reduces the amount of information required in the images [3]. The bistatic radiometer (BR), as a spaced radiometric device, can detect and measure the difference in the movement of the RP antennas during its travel [4, 5], thereby increasing the amount of necessary information in the images. Also, the BR detects and measures the difference Doppler frequency correction of mapping objects [6].

The images obtained using BR have significant advantages over single-channel and matrix radiometric systems [7, 8].

Thus, determining the parameters of radiometric images during remote sensing of various earth surfaces (covers) is an urgent scientific task.

**Analysis of research and publications.** The results of the studies presented in the well-known literature do not provide an opportunity to determine the parameters of radiometric images. At the same time, the technical characteristics of the bistatic radiometer [9, 10], changes in

its range [11, 12], surface viewing sector [13, 14], image band [15, 16], etc. are not considered.

Also, the differences in motion and the difference Doppler frequency of useful signals are not measured [17–19]. These publications provide only approaches to solving this problem, but do not define and analyse the parameters of radiometric images regarding the technical characteristics of the BR.

**The aim of the article** is to develop a numerical simulation methodology for enhancing the amount of information on radiometric images during remote sensing of various earth surfaces (covers) depending on the technical characteristics of the BR.

### Summary of the main material

In remote earth surface sensing, the main information of the system is the acquired images, which are technically feasible. In the 3-mm wavelength range, the input bandwidth of the BR is 22 GHz [20]. Such a large input bandwidth of the BR determines the distinguishing ability by the difference in the stroke on the mapping surface and positively affects the fluctuation sensitivity of the system.

The low-contrast radiometric signal grass-concrete was chosen as a useful signal. It is proposed to use the

AN-14 'Bee' passenger aircraft for the mapping.

The main characteristics of the mapping system include the range and bandwidth of the radiometric image [21].

**1. Numerical modelling of the BR range values for mapping various earth surfaces:**  $R(S, T, Bw_o, Bw_d)$  [22].

There are known theoretical and experimental studies of various earth covers at horizontal polarisation and  $40^\circ$  receiving angle at wavelengths of 2.15 mm and 8 mm. Large-scale modelling has provided approximate radio luminance temperatures of grass and concrete land covers and the grass-concrete contrast [23].

So, we can write the following:

$$\Delta_{2,7} = 0,5 \left( \Delta_{2,15} \sqrt{\frac{\lambda}{\lambda_{2,15}}} + \Delta_8 \sqrt{\frac{\lambda}{\lambda_8}} \right), \quad (1)$$

where  $\Delta_{2,7}$  – is the radio luminance contrast 'grass-concrete' at the BR wavelength  $\lambda = 2,7$  mm;  $\Delta_{2,15}, \lambda_{2,15}$  – are the contrast 'grass-concrete' at  $\lambda = 2,15$  mm and the wavelength  $\lambda = 2,15$ ;  $\Delta_8, \lambda_8$  – are the contrast 'grass-concrete' at  $\lambda = 8$  mm and the wavelength  $\lambda = 8$  mm.

According to the results of the calculations (1), we obtained:  $\Delta_{2,7} \approx 29$  K, as well as the radiant temperatures of concrete  $T_{\text{concrete}} \approx 267$  K and grass  $T_m \approx 296$  K. The range of the BR for mapping earth surfaces is equal to [23]:

$$R(S, T, Bw_o, Bw_d) = \sqrt{\frac{(1-\beta) \left[ T - [T_{rl} C + T_{atm}(\phi, B, R)] \right] SG}{4\pi\alpha_1\gamma(Bw_o, Bw_d)L[T_0(K-\eta) + A]}}, \quad (2)$$

$$C = \exp(-0,23BR_a),$$

where  $S, T$  – are, respectively, the square of the mapped object and its radio luminous temperature ( $S$  varies from  $1 \text{ m}^2$  to  $4 \cdot 10^2 \text{ m}^2$ ,  $T$  – from  $130 \text{ K}$  to  $320 \text{ K}$ );  $Bw_o, Bw_d$  – are, accordingly, the bandwidth of the BR output filter and the bandwidth of the BR output Doppler RC filter (during the simulation, the bands were changed from  $1 \text{ Hz}$  to  $1 \text{ kHz}$ );  $\beta$  – is a coefficient that accounts for the reception of signals outside the main lobe of the RP antennas ( $0.31$  is assumed);  $T_{rl}$  is the radio luminous temperature of the mapping surface (grass  $\sim 296 \text{ K}$ );  $C$  – is the atmospheric quality factor;  $T_{atm}(\phi, B, R)$  – is the radiant temperature of the atmospheric layer between the mapping surface and the BR ( $K$ );  $\phi$  – is the zenith angle of the system ( $0^\circ$  is chosen);  $B$  – is the absorption coefficient of radiometric signals in the presence of oxygen and water vapour ( $7.5 \text{ g/m}^3$ ) in the atmosphere (provided everything is clear, then  $B \approx 0,73 \text{ dB/km}$  and with rain of  $4 \text{ mm/h}$ , then  $B \approx 1.57 \text{ dB/km}$ );  $R_a$  – is the distance to the mapping objects in kilometres (km);  $G$  – is the BR antenna gain coefficient;  $\alpha_1, L$  – are the BR constant and the losses in the mapping system,

respectively ( $\alpha_1 = \sqrt{2}$ ,  $L = 2$  times);  $\gamma(Bw_o, Bw_d)$  – is the ratio of the average useful signal powers to the intrinsic noise in the BR channels;  $K_n, \eta$  – are the noise coefficient of the BR channels and the BR antenna efficiency, respectively ( $K_n = 3$ ,  $\eta = 0,78$ ). In this case:

$$T_{atm}(\phi, B, R_a) \approx T_0 \left\langle 1 - 1/\left\{ \exp\left[0,23BR_a/\cos\phi\right] \right\} \right\rangle$$

$$G \approx 3,2 \cdot 10^4 D^2 \left[ \lambda(180/\pi) \right]^{-2}, \quad \gamma(Bw_o, Bw_d) =$$

$$= \frac{\nu(Bw_o, Bw_d) + \sqrt{\nu(Bw_o, Bw_d) \left[ \frac{Rt_c(Bw_o) - \nu(Bw_o, Bw_d)}{-\nu(Bw_o, Bw_d)} \right]}}{Rt_c(Bw_o) - 2\nu(Bw_o, Bw_d)}, \quad (3)$$

$$A = \eta \left[ T_{atm}(\phi, B, R_a) + t_3 C + (1-\beta) \times \right.$$

$$\left. \times \sum_{i=1}^n t_i C \delta_i + \beta \sum_{j=1}^k t_j C \delta_j \right],$$

where  $T_0$  is the absolute temperature at the earth's surface ( $290 \text{ K}$ );  $D$  is the diameter of the BR reflector antennas ( $0.31 \text{ m}$  is taken);  $\lambda$  is the central wavelength of the BR ( $2.7 \text{ mm}$  is chosen);  $\nu(Bw_o, Bw_d)$  is the signal-to-noise ratio (s/n) at the output of the BR at a fixed coherent accumulation time;  $Rt_c(Bw_o)$  is the compression ratio of radiometric signals in the BR;  $t_i, t_j$  are, respectively, the radio luminous temperatures of interference ('mapping surface') located in the main lobes of the RP antennas  $i = 1, 2 \dots n$  and side lobes of RP antennas  $j = 1, 2 \dots k$ ;  $\delta_i, \delta_j$  – are, respectively, solid angles of mapping objects in the main lobes and side lobes of RP antennas of BR.

Thus, we can state the following:

$$\nu(Bw_o, Bw_d) = \left[ \nu_1 L_s(Bw_o, Bw_d) \right] / 0,9514,$$

$$R_t(Bw_d) = 3Bw_{in} Bw_o^{-1}, \quad P = 1 - F^{(1+\nu_1)^{-1}}, \quad (4)$$

where  $\nu_1$  is the s/n ratio, at which the probability of accurate detection of the object  $P = 0,5$ , provided that the probability of false alarm  $F = 10^{-1}$  ( $\nu_1 = 2,32$  times was chosen);  $L_s(Bw_o, Bw_d)$  – losses in the ratio of s/n due to insufficient accumulation time of useful signals;  $0,9514$  – indicates losses in the ratio of s/n when limiting the accumulation time at the level of  $3Bw_o^{-1}$ ;  $Bw_{in}$  – input bandwidth of the BR ( $22 \text{ GHz}$  is accepted). In turn:

$$L_s(Bw_o, Bw_d) = \left[ q_1(Bw_o) / q_2(Bw_o, Bw_d) \right]^2,$$

$$t(Bw_o) = 3Bw_o^{-1}, \quad m_1(Bw_o) = 1 - \exp[-Bw_o t(Bw_o)],$$

$$\sigma_1(Bw_o) = \sqrt{1 - \exp[-2Bw_o t(Bw_o)]},$$

$$q_1(Bw_o) = m_1(Bw_o) / \sigma_1(Bw_o), \quad (5)$$

$$m_2(Bw_o, Bw_d) = 1 - \exp[-Bw_d t(Bw_o)],$$

$$\sigma_2(Bw_o, Bw_d) = \sqrt{1 - \exp[-2Bw_d t(Bw_o)]},$$

$$q_2(Bw_o, Bw_d) = m_2(Bw_o, Bw_d) / \sigma_2(Bw_o, Bw_d),$$

where  $q_1(Bw_o), q_2(Bw_o, Bw_d)$  are respectively the ratio of the s/n, which is matched to the bandwidth of the output RC filter of the BR and the ratio of the s/n at their output, when measuring the difference Doppler frequency correction of the mapping objects;  $t(Bw_o)$  – time for coherent accumulation of useful signals;  $m_1(Bw_o), \sigma_1(Bw_o)$  – respectively, the mathematical expectation (ME) of a random process and its root mean square deviation (RMSD) of errors at the output of the BR output filter;  $m_2(Bw_o, Bw_d), \sigma_2(Bw_o, Bw_d)$  – respectively, the ME of a random process and its RMSD of errors for the output Doppler filters.

The mapping object is concrete on a grass background with a radiant surface contrast of  $\sim 29K$  (1). The radiant temperature of concrete  $T_{conc}$  increases due to the influence of the atmosphere:

$$T_{conc} \approx (T_s - 29)C + T_{atm}(\phi, B, R_a), \quad (6)$$

provided that  $\phi = 0^\circ$ ,  $B \approx 0,73$  dB/km and  $R_a \approx 2,7$  km –  $T_{conc} \approx 276$  K is obtained. In this case, if  $S = 10^2$  m<sup>2</sup> and  $Bw_o = Bw_d = 10^3$  Hz, then:

$$t(10^3) = 3 \cdot 10^{-3} \text{ s}, \quad q_1(10^3) = 0,9514, \quad A \approx 343,9 \text{ K};$$

$$\nu(10^3, 10^3) \approx 2,44, \quad K_c(10^3) \approx 7,33 \cdot 10^6,$$

$$G \approx 1,29 \cdot 10^5, \quad C \approx 0,625; \quad \gamma(10^3, 10^3) \approx 0,58 \cdot 10^{-3};$$

$$T_{atm}(0; 0,73; 2,8) \approx 108,77 \text{ K}, \quad \delta_i \approx 0,22, \quad \delta_j = 1.$$

According to the calculations, we obtained:

$$R(10^2; 276; 10^3; 10^3) \approx 2791 \text{ m}.$$

According to the data obtained, the first curve  $R_1(T)$ , was constructed, which is shown in Fig. 1 and is marked with a dash. For the grass-water contrast, we should expect  $R_1(254) \approx 4188$  m, with  $\delta_i \approx 0,22$ . With an average rainfall of 4 mm/h, the range of the BR decreases by a factor of 1,16 and is (for a grass-concrete object)  $R_1(280) \approx 2399$  m, with  $\delta_i \approx 0,32$ . There are significant losses in the range of the BR when absorbing radio waves by the atmosphere.

Provided that the differential Doppler correction of the BR frequency is detected, the bandwidth of the output filter  $Bw_d$  – is reduced from  $10^3$  to 20 Hz. That is why, it is proposed to use a constant time for the accumulation of useful signals  $t(10^3) = 3 \cdot 10^{-3}$  s when detecting the grass-concrete contrast. Provided that:

$$\phi = 0^\circ, \quad B \approx 0,73 \text{ dB/km}, \quad R_a \approx 1,4 \text{ km}; \quad T_{conc} \approx 272 \text{ K}.$$

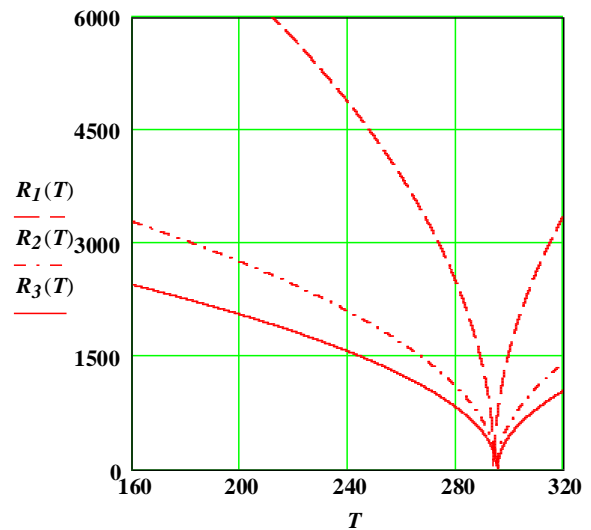


Fig. 1. Ranges of a bistatic radiometer for mapping earth surfaces  $R_i(T)$  depending on the radio luminous temperature of the object  $T$

According to the results of the calculations, the following were obtained:

$$L_s(10^3, 20) \approx 30,18, \quad \nu(10^3, 20) \approx 73,66, \quad C \approx 0,79,$$

$$T_{atm}(0; 0,73; 1,4) \approx 60,75 \text{ K}, \quad \gamma(10^3, 20) \approx 3,18 \cdot 10^{-3},$$

$$\delta_i \approx 0,52, \quad \delta_j = 1, \quad A \approx 340,6 \text{ K};$$

$$R(10^2; 272; 10^3; 20) \approx 1349 \text{ m}.$$

When detecting the grass-water contrast  $R_2(232) \approx 2240$  m should be expected when  $\delta_i \approx 0,52$ , this is the second  $R_2(T)$  curve, which is marked with dots and dashes (Fig. 1).

To measure the difference in stroke between the BR receiving points and the Doppler frequency correction, the ratio of the s/n at the system output  $\nu_1$  should be increased from  $\sim 2,32$  to 32 times. The increase in the s/n leads to a major loss of the mapping system range. Improvement of the range is possible by using of BR input amplifiers with a noise figure of  $\sim 1,34$  (70K) [24, 25].

Consequently, we should expect at:

$$t(10^3) = 3 \cdot 10^{-3} \text{ s}, \quad B \approx 0,73 \text{ dB/km}, \quad R_a \approx 1,1 \text{ km},$$

$$B_m(10^3, 20) \approx 30,18, \quad \nu(10^3, 20) \approx 1015, \quad C \approx 0,83,$$

$$T_{conc} \approx 271 \text{ K}, \quad T_{atm}(0; 0,73; 1,1) \approx 48,91 \text{ K},$$

$$\gamma(10^3, 20) \approx 11,9 \cdot 10^{-3}, \quad \delta_i \approx 0,82, \quad \delta_j = 1, \quad A \approx 331,6 \text{ K}$$

operating range:  $R(10^2; 271; 10^3; 20) \approx 1031$  m.

When measuring the stroke difference and Doppler frequency correction, for the grass-water contrast, we obtained:  $R_3(229) \approx 1710$  m, when  $\delta_i \approx 0,82$  – the third curve  $R_3(T)$ , which is marked with a continuous line (Fig. 1).

Thus, according to the accepted technical characteristics of the BR, the detection of low-contrast objects only by the difference in stroke gives the greatest range of  $\sim 2,8$  km. Detection by the difference in stroke and Doppler frequency correction, with a fixed time to accumulate useful signals of 3 ms, reduces the range of the BR to  $\sim 1,3$  km. Measurement of the stroke difference and Doppler frequency correction also requires a significant s/n ratio at the system output, which reduces the range of the BR to  $\sim 1,0$  km at a fixed time for accumulation of useful signals of 3 ms.

## 2. Numerical simulation of values of radiometric image bands of land cover II and difference Doppler frequency correction of mapping objects [25].

The radio luminous contrast of grass-concrete was considered as a low-contrast payload. An AN-14 'Bee' aircraft with a flight speed of  $V_h = 50$  m/s. was chosen as a BR carrier. The assumed distance between the BR reception points (system base, B) is  $\approx 10$  m.

2.1. In the numerical simulation, the viewing sector of the surfaces  $\alpha_o \sim \pm 50^\circ$ , or ranges from  $0^\circ$  to  $60^\circ$ . The system's scanning speed is constant. After  $t(Bw_o)$  of 3 ms, the output filters of the BR are read out and the accumulated signals are nullified. The image band consists of the antenna system steps  $K_i$ , which are obtained by accumulating useful signals in 3 ms. The first row of the radiometric image band  $Bw$  is equal to:

$$\begin{aligned} Bw &= I_1 + I_2 + I_3 + I_4 \dots + I_n, \\ Cr &= R(S, T, Bw_o, Bw_d) \cos \alpha_o, \quad \Theta \approx \sqrt{2\lambda/D}, \\ I_1 &= Cr \cdot tg(\Theta/2) - B, \\ I_2 &= \sqrt{I_1^2 + Cr^2} \sin \Theta / \sin[\pi/2 - \text{artg}(I_1/Cr) - \Theta], \quad (7) \\ I_3 &= \frac{\sqrt{(I_1 + I_2)^2 + Cr^2} \sin \Theta}{\sin\{\pi/2 - \text{artg}[(I_1 + I_2)^2/Cr] - \Theta\}}, \\ I_4 &= \frac{\sqrt{(I_1 + I_2 + I_3)^2 + Cr^2} \sin \Theta}{\sin\{\pi/2 - \text{artg}[(I_1 + I_2 + I_3)^2/Cr] - \Theta\}}, \end{aligned}$$

where  $I_i$  – are image steps,  $i = 1, 2 \dots n$ ;  $Cr$ ,  $\alpha_o$  – respectively, the carrier flight altitude and the viewing sector of the earth surfaces;  $\Theta$  – half-width of the RP of the BR antennas ( $\Theta \approx 1,23 \cdot 10^{-2}$  rad).

The second and subsequent image rows are generated after the carrier has passed the diameter of the signal reception spot, at a zenith angle of  $\phi = 0^\circ$ . The time to generate an image row  $t_r$  and the number of steps  $I_{st}$  can be defined as follows:

$$t_p = 2[Cr \cdot tg(\Theta/2)]V_h^{-1}, I_{st} = [t_r/t(\Pi_o)]. \quad (8)$$

According to the equation of the hyperboloid rotation  $y(r, x)$  [24] it is possible to calculate the

distance between the differences in the path of useful signals on the mapping surface:

$$y(r, x) = \sqrt{(1 - 4x^2/r^2)(0,25r^2 - B)}, \quad r = \frac{2nc}{Bl}, \quad (9)$$

where  $r$  – is the path difference of the useful signals between the receiving points of the BR (along the line of the base B  $r = 1,36 \cdot 10^{-2}$  m);  $n, c$  – are, respectively, the number of the path difference ( $n = 0, 1, 2 \dots 10$ ) and the light speed  $c = 3 \cdot 10^8$  m/s.

According to the calculations in (7), (8) and at  $R(10^2; 276; 10^3; 10^3) \approx 2791$  m, the image band  $Bl \approx 3588$  m was also obtained:

$$\text{if } R(10^2; 272; 10^3; 20) \approx 1349 \text{ m, then } Bl \approx 663 \text{ m;}$$

$$\text{if } R(10^2; 271; 10^3; 20) \approx 1013 \text{ m, then } Bl \approx 212 \text{ m.}$$

The length of the radiometric image during the flight of the carrier is determined by the memory capacity of the mapping system.

2.2. Calculation of the difference Doppler frequency correction of objects on the mapping surface  $F_p(V_o, \mu, S, T, Bw_o, Bw_d, Bw)$  [26, 27].

Provided that the object velocity vector  $V_o$  (ground wind speed) and the carrier velocity vector  $V_h$  the dynamic velocity vector of the mapping object  $V_d(V_o, \mu)$  can be calculated using the following method:

$$V_d(V_o, \mu) = \sqrt{V_o^2 + V_h^2 - 2V_oV_h \cos(\pi - \mu)}, \quad (10)$$

where  $\mu$  – is the angle between the vectors  $V_h$  and  $V_o$  (in numerical modelling, it varies from 0 to  $2,5\pi$ ).

The angle between the vectors  $V_h$  and  $V_d(V_o, \mu)$ , denoted by  $\theta(V_o, \mu)$  and the projection of the dynamic velocity of the object onto the mapping plane  $V_{pl}(V_o, \mu)$  can be obtained by the following expressions:

$$\begin{aligned} \theta(V_o, \mu) &= \\ &= \text{acos}\left\{\left[\frac{V_h^2 + V_d(V_o, \mu)^2 - V_o^2}{2V_hV_d(V_o, \mu)}\right]\right\}, \quad (11) \end{aligned}$$

$$V_{pl}(V_o, \mu) = V_d(V_o, \mu) \cos[0,5\pi - \theta(V_o, \mu)].$$

The value of the difference Doppler frequency correction of the objects  $F_c(V_o, \mu, S, T, Bw_o, Bw_d, Bl)$  and the required number of Doppler filters at the output of each stroke difference  $N_d(V_o, \mu, S, T, Bw_o, Bw_d, Bl)$  can be calculated as follows:

$$\begin{aligned} F_c(V_o, \mu, S, T, Bw_o, Bw_d, Bl) &= 2V_{pl}(V_o, \mu)/\lambda_2 \times \\ &\times \sin\left[\left(\beta(S, T, Bw_o, Bw_d, Bl) + \alpha(S, T, Bw_o, Bw_d, Bl)\right)/2\right] \times \\ &\times \sin\left(\gamma(S, T, Bw_o, Bw_d, Bl)/2\right), \\ \gamma(S, T, Bw_o, Bw_d, Bl) &= \quad (12) \end{aligned}$$

$$= \beta(S, T, Bw_o, Bw_d, Bl) - \alpha(S, T, Bw_o, Bw_d, Bl),$$

$$N_d(V_o, \mu, S, T, Bw_o, Bw_d, Bl) =$$

$$= F_c(V_o, \mu, S, T, Bw_o, Bw_d, Bl) / Bw_d,$$

where  $\beta(S, T, Bw_o, Bw_d, Bw)$  – is the angle between the first BR receiving point, the object and the image row;  $\alpha(S, T, Bw_o, Bw_d, Bw)$  – is the angle between the second receiving point, the object and the image row.

The results of numerical modelling of the values of the differential Doppler frequency correction are shown in Fig. 2, provided that:  $R(10^2; 272; 10^3; 20) \approx 1349$  m,  $Bw_o = 10^3$  Hz,  $Bw_d = 20$  Hz and  $Bl \approx 663$  m.

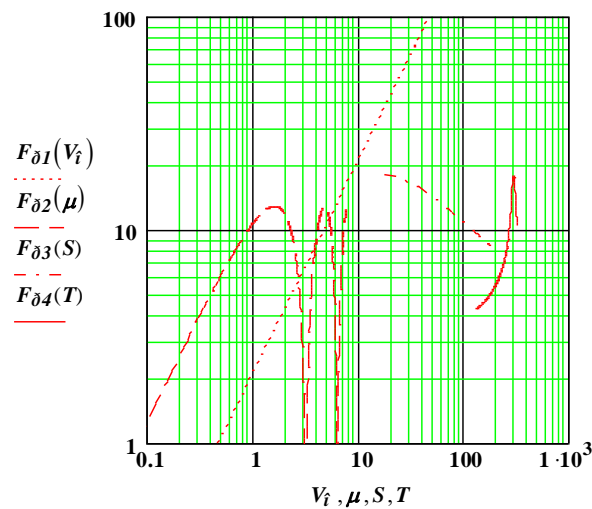


**Fig. 2.** The value of the difference Doppler frequency correction of the mapping objects  $F_{\delta}(z)$  depending on the variables  $V_o, \mu, S$  and  $T$

The first curve  $F_{\delta 1}(V_o)$  is marked with points and is obtained when the object's velocity  $V_o$  changes and at:  $\mu = 1$ ,  $S = 10^2$  m<sup>2</sup>,  $T = 272$  K. The second curve  $F_{\delta 2}(\mu)$  (dash) shows the Doppler frequency at different values of  $\mu$  from 0 to  $2,5\pi$ . It is noted that it is impossible for the system to detect the difference Doppler frequency correction if  $\mu$  is close to  $\pi, 2\pi$ . The curve  $F_{\delta 2}(\mu)$  was calculated at:  $V_o = 5$  m/s,  $S = 10^2$  m<sup>2</sup>,  $T = 272$  K. The third curve  $F_{\delta 3}(S)$  (dots and dashes) was plotted at different planes of the mapping objects at:  $\mu = 1$ ,  $V_o = 5$  m/s,  $T = 272$  K. The increase in the square  $S$  leads to an increase in the range of the system and a significant decrease in the angle  $\gamma(S, T, Bw_o, Bw_d, Bl)$ , which explains the decrease in the values of  $F_{\delta 3}(S)$ . The fourth curve  $F_{\delta 4}(T)$  (continuous) was calculated when mapping various radio luminous objects. The lack of contrast between the grass and the object leads to a loss of the system's range and an increase in the angle  $\gamma(S, T, Bw_o, Bw_d, Bw)$ , which explains the increase in  $F_{\delta 4}(T)$  values.

### 3. Numerical modelling for optimisation of radiometric image characteristics of various land covers.

Six options for building the system are considered. The image characteristics include:

- 1) band (line length) of the image  $Bl$ ;
- 2) number of RP steps of the BR antenna system  $N_{st}$ ;
- 3) the number of pixels (stroke differences) on the image row  $n_{px}$ ;
- 4) resolution along the carrier's flight path  $P_{ry}$  and crosswise  $P_{rx}$  at the carrier and zenith angle  $0^\circ$ ;
- 5) is the difference Doppler frequency correction resolution  $P_{r F_d}$ ;

6) number of Doppler filters at the output of each of the stroke differences  $N_{di}$ , provided that the speed of the mapping object is 30 m/s;

RMSD for measuring the stroke difference  $\sigma_\tau$  and RMSD for measuring the difference Doppler frequency correction  $\sigma_{F_\delta}$  [28, 29]:

$$\sigma_\tau(Bw_{in}, v_1) = \sqrt{3}c / (\pi Bw_{in} v_1),$$

$$\sigma_{F_\delta}(Bw_d, v_1) = \sqrt{3}Bw_d / (\pi v_1).$$
(13)

Fluctuation sensitivity of the BR  $T_{fl}$  [30]:

$$fl = \alpha_1(T_{rec} + T_{ant}) / \sqrt{Bw_{in} Bw_f^{-1}}, \quad T_{rec} = T_0(N_{st} - 1), \quad (14)$$

where  $T_{rec}$  – is the temperature of the BR receiving channel ( $\sim 580$  K and  $\sim 99$  K were obtained in the numerical modelling);  $Bw_f$  – is the bandwidth of the BR output filter ( $10^3$  Hz and 20 Hz were taken).

**3.1.** According to the first design option, the surface mapping is carried out in the sector  $\alpha_o \pm 40^\circ$  from the zenith angle.

According to the results of the calculations, we obtained:  $R(10^2; 276; 10^3; 10^3) \approx 2791$  m,  $Bl \approx 3588$  m,  $N_{st} = 170$ ,  $n_{px} = 554$ ,  $P_{ry} \approx 26,3$  m,  $P_{rx} \approx 5,8$  m,  $\sigma_\tau \approx 0,3$  m and  $T_{fl} \approx 0,15$  K. When expanding the RP of the BR antennas, the value of  $Bl$  decreases and the number of  $n_{px}$  increases.

Expanding the RP of the BR antennas by  $\sim 1,8$  times reduces the range from 2791 m to 1710 m and reduces the image band from 3588 m to 2820 m. Although, at the same time, the number of pixels per line increases from 554 to 870.

**3.2.** The second variant of the system design provides a side view of the surfaces,  $\alpha_o$  varies from  $0^\circ$  to  $\sim 55^\circ$ .

According to the results of the calculations, we obtained:  $R(10^2; 276; 10^3; 10^3) \approx 2791$  m,  $Bl \approx 2254$  m,  $N_{st} = 129$ ,  $n_{px} = 480$ ,  $P_{ry} \approx 19,7$ ,  $P_{rx} \approx 4,4$  m,  $\sigma_\tau \approx 0,3$  m and  $T_{fl} \approx 0,15$  K.

**3.3.** The third variant of the system implementation detects the difference in the stroke and the difference Doppler frequency correction of the mapping objects, with a viewing sector of  $\alpha_o \pm 15^\circ$  from the zenith angle of  $0^\circ$ .

According to the results of the calculations, the following were obtained:  $R(10^2; 272; 10^3; 20) \approx 1349$  m,  $Bl \approx 663$  m,  $N_{st} = 106$ ,  $n_{px} = 106$ ,  $P_{ry} \approx 16$  m,  $P_{rx} \approx 3,6$  m,  $P_{rV} \approx 9,3$  m/s,  $N_{di} = 4$ ,  $\sigma_\tau \approx 0,3$  m,  $\sigma_{Fd} \approx 5,1$  H. The fact that  $Bw_d$  decreased from  $10^3$  Hz to 20 Hz, the sensitivity of the system improved, so  $T_{fl} \approx 0,02$  K.

**3.4.** According to the fourth design option, the mapping surface view sector provides a lateral view of the surface,  $\alpha_o$  varies from 0 to  $28^\circ$ . According to the numerical modelling results, we obtained:  $R(10^2; 272; 10^3; 20) \approx 1349$  m,  $Bl \approx 576$  m,  $N_{st} = 97$ ,  $n_{px} = 132$ ,  $P_{ry} \approx 15$  m,  $P_{rx} \approx 3,3$  m,  $P_{rFd} \approx 9,1$  m/s,  $N_{di} = 4$ ,  $\sigma_\tau \approx 0,3$  m,  $\sigma_{Fd} \approx 5,1$  Hz and  $T_{fl} \approx 0,02$  K.

**3.5.** Measurement of the stroke difference and difference Doppler frequency correction, as mentioned earlier, is possible with an increase in the s/n ratio  $\nu_1$  from 2,32 times to 32 times and an improvement in the noise floor of the receiving channels from 3 to 1.34 times.

With a viewing sector of space  $\alpha_o \pm 6^\circ$  from the zenith angle, the results of numerical simulation obtained:  $\nu_1 = 32$ ,  $Rt_{st} = 1,34$ ,  $R(10^2; 271; 10^3; 20) \approx 1034$  m,  $Bl \approx 212$  m,  $N_{st} = 84$ ,  $n_{px} = 84$ ,  $P_{ry} \approx 12,6$  m,  $P_{rx} \approx 2,8$  m,  $P_{rFd} \approx 6,7$  m/s,  $N_{di} = 5$ ,  $\sigma_\tau \approx 10^{-3}$  m,  $\sigma_{Fd} \approx 1,4$  Hz. By reducing the noise floor, the value of  $T_{fl}$  is reduced to  $9,3 \cdot 10^{-3}$  K.

**3.6.** According to the sixth design option, the system performs a lateral view of the surfaces,  $\alpha_o$  varies from  $0^\circ$  to  $12^\circ$ .

According to the numerical modelling results, we obtained:  $Rt_{st} = 1,34$ ,  $R(10^2; 271; 10^3; 20) \approx 1029$  m,  $\nu_1 = 32$ ,  $Bl \approx 205$  m,  $N_{st} = 82$ ,  $n_{px} = 82$ ,  $P_{ry} \approx 12,4$  m,  $P_{rx} \approx 2,75$  m,  $P_{rFd} \approx 6,7$  m/s,  $N_{di} = 5$ ,  $\sigma_\tau \approx 10^{-3}$  m,  $\sigma_{Fd} \approx 1,4$  Hz and  $T_{fl} \approx 9,3 \cdot 10^{-3}$  K.

Thus, based on the numerical modelling, six options for radiometric images were obtained, which are feasible according to the accepted technical characteristics. To consider the possibilities of detecting objects by the difference in stroke and the difference Doppler frequency

correction. An analysis of the information amount in the images when measuring the difference in stroke and difference Doppler frequency correction of mapping objects is carried out.

## Conclusions

Thus, according to the criteria of the largest number of pixels in the image row and image band, the best construction option is the first variant, where  $n_{px} = 554$  and  $Bl = 3588$  m. In this case, the resolution of the system along the carrier's flight path  $P_{ry} \sim 26,3$  m and across it  $\sim 5,83$  m are the worst obtained in the numerical modelling. Although, with a viewing sector of up to  $\pm 40^\circ$  a significant difference in the radiative capacity of various earth surfaces is not used.

The second variant has a viewing sector from  $0^\circ$  to  $55^\circ$ , which leads to better detection of various objects. The resulting losses, as compared to the first variant, are  $n_{px}$  up to 480 and  $Bl = 2254$  m. The resolution is slightly better, with  $P_{ry}$  of  $\sim 19,7$  m along the flight path and  $P_{rx}$  of  $\sim 4,4$  m across it. Detection of objects by differential Doppler frequency correction according to the III and IV construction variants improves the fluctuation sensitivity of the BR  $T_{fl}$  from  $\sim 0,15$  K to  $\sim 0,02$  K. During the numerical modelling, we obtained a reduction of  $n_{px}$ , considering Doppler filters, to 424 and the loss of image bandwidth, relative to the first variant, was  $\sim 5,4$  times. The resolution of  $P_{ry}$ ,  $P_{rx}$  respectively, improves to  $\sim 16$  m and  $\sim 3,6$  m, and the speed resolution is only  $\sim 9,3$  m/s. At the same time, the RMSD in stroke  $\sigma_\tau \sim 0,3$  m and the RMSD in Doppler frequency correction of  $\sigma_{Fd} \sim 5,1$  Hz. Measurements of the stroke difference and the differential Doppler frequency correction (V, VI variants) led to a significant reduction in the image bandwidth, as compared to the first construction variant, by  $\sim 17$  times. The number of pixels, including Doppler filters, is  $\sim 420$ .

The resolution of  $P_{ry}$ ,  $P_{rx}$  respectively, improves to  $\sim 12,5$  m and  $\sim 2,8$  m. The speed resolution, relative to the III and IV design variants, decreases from  $\sim 9,3$  m/s to  $\sim 6,7$  m/s.

The main advantage of the V and VI design variants, in comparison with the previous ones, is the lowest fluctuation sensitivity of the BR  $T_{fl} \sim 9,3 \cdot 10^{-3}$  K and the RMSD in stroke  $\sigma_\tau \sim 10^{-3}$  m and the RMSD in Doppler frequency correction of objects  $\sigma_{Fd} \sim 1,4$  Hz.

Based on the results of numerical modelling, we analysed the amount of information on radiometric images during remote sensing of earth surfaces by an on-board system that is spaced.

## REFERENCES

1. Liu, J., Zhang, R., Sun, G., Yu, Z., Gao, W. and Liu, Y. (2023), "Design and implementation of high sensitivity microwave radiometer", *AEU – Int. Journal of Electronics and Communications*, 170, doi: <https://doi.org/10.1016/j.aeue.2023.154800>
2. Dong, J., Li, Q., Shi, R., Gui, L. and Guo, W. (2011), "The placement of antenna elements in aperture synthesis microwave radiometers for optimum radiometric sensitivity", *IEEE Transactions on Antennas and Propagation*, vol. 59(11), pp. 4103–4114, no. 5979146, doi: <https://doi.org/10.1109/TAP.2011.2164172>

3. Lukin, K.A., Kudriashov, V.E., Vyplavin, P.L. and Palamarchuk, V.P. (2014), "Coherent imaging in the range-azimuth plane using a bistatic radiometer based on antennas with beam synthesizing", *IEEE Aerospace and Electronic Systems Magazine*, vol. 29, is. 7, pp. 16–22, doi: <https://doi.org/10.1109/MAES.2014.130142>
4. Kudriashov, V.E. (2015), "A Modified Maximum Likelihood Method for Estimation of Mutual Delay and Power of Noise Signals by Bistatic Radiometer", *Comptes Rendus - Academie Bulgarie des Sciences*, vol. 68, no. 5, pp. 631–640, available at: <https://go.gale.com/ps/i.do?id=GALE%7CA570688267&sid=googleScholar&v=2.1&it=r&linkaccess=abs&issn=13101331&p=AONE&sw=w&userGroupName=anon%7E545e1579&atv=open-web-entry>
5. Kudryashov, V.E. (2018), "A Bistatic Radiometry System for Object Mapping", *Telecommunications and Radio Engineering*, Begell House, vol. 77, iss. 20, pp. 1813–1826, doi: <https://doi.org/10.1615/TelecomRadEng.v77.i20.40>
6. Kudryashov, V., Litovchenko, D. and Filippenkov, O. (2020), "Multi – channel reception system for radiometry signals", *IEEE, Ukrainian Microwave Week*, Kharkiv, pp. 318–322, doi: <https://doi.org/10.1109/ukrmw49653.2020.9252699>
7. Ivanov, V.K. and Yatsevich, S.E. (2008), "Development of methods of remote sensing of the earth at the IRE NAS of Ukraine", *Radiofizika i Elektronika*, vol. 13, pp. 333–343, available at: <http://dspace.nbu.gov.ua/handle/123456789/10762>
8. Hunko, M., Tkachov, V., Kuchuk, H., Kovalenko, A. (2023), Advantages of Fog Computing: A Comparative Analysis with Cloud Computing for Enhanced Edge Computing Capabilities, *2023 IEEE 4th KhPI Week on Advanced Technology, KhPI Week 2023 – Conf. Proc.*, 02-06 October 2023, Code 194480, doi: <https://doi.org/10.1109/KhPIWeek61412.2023.10312948>
9. Le Vine, D.M. and De Matthaeis, P. (2024), "Characteristics of RFI Determined From Kurtosis Using the SMAP Radiometer", *IEEE Transactions on Geoscience and Remote Sensing*, 62, pp. 1–11, doi: <https://doi.org/10.1109/TGRS.2023.3338964>
10. Petrovska, I., Kuchuk, H., Kuchuk, N., Mozhaiev, O., Pochebut, M. and Onishchenko, Yu. (2023), "Sequential Series-Based Prediction Model in Adaptive Cloud Resource Allocation for Data Processing and Security", *2023 13th International Conference on Dependable Systems, Services and Technologies, DESSERT 2023*, 13–15 October, Athens, Greece, code 197136, doi: <https://doi.org/10.1109/DESSERT61349.2023.10416496>
11. Lukin, K.A., Kudriashov, V.V., Vyplavin, P.L., Palamarchuk, V.P. and Lukin, S.K. (2015), "Coherent radiometric imaging using antennas with beam synthesizing", *International Journal of Microwave and Wireless Technologies*, vol. 7, iss. 3–4, pp. 453–458, doi: <https://doi.org/10.1017/S1759078715000550>
12. Kuchuk, H. and Malokhvii, E. (2024), "Integration of IOT with Cloud, Fog, and Edge Computing: A Review", *Advanced Information Systems*, vol. 8(2), pp. 65–78, doi: <https://doi.org/10.20998/2522-9052.2024.2.08>
13. Tenerelli, J.E., Reul, N., Mouche, A.A. and Chapron, B. (2008), "Earth-viewing L-band radiometer sensing of sea surface scattered celestial sky radiation - Part I: General characteristics", *IEEE Transactions on Geoscience and Remote Sensing*, vol. 46(3), pp. 659–674, no. 4447249, doi: <https://doi.org/10.1109/TGRS.2007.914803>
14. Petrovska, I., Kuchuk, H. and Mozhaiev, M. (2022), "Features of the distribution of computing resources in cloud systems", *2022 IEEE 4th KhPI Week on Advanced Technology, KhPI Week 2022 - Conference Proceedings*, 03–07 October 2022, Code 183771, doi: <https://doi.org/10.1109/KhPIWeek57572.2022.9916459>
15. Kudryashov, V.V., Lukin, K.A., Palamarchuk, V.P. and Vyplavin, P.L. (2013), "Coherent radiometric imaging with a Ka-band ground-based synthetic aperture noise radar", *Telecommunications and Radio Engineering*, 2013, vol. 72, no. 8, pp. 699–710, <https://doi.org/10.1615/TelecomRadEng.v72.i8.50>
16. Kuchuk, N., Mozhaiev, M., Kalinin, Y., Mozhaev, O. and Kuchuk, H. (2022), "Calculation of Signal Information Delay in Intelligent Communication Networks", *2022 IEEE 3rd KhPI Week on Advanced Technology, KhPI Week 2022 - Conference Proceedings*, doi: <https://doi.org/10.1109/KhPIWeek57572.2022.9916323>
17. Singh, R., Czaplá-Myers, J. and Anderson, N. (2022), "Ground viewing radiometer equipped with autonomous linear motion: Two Year field deployment summary and analysis", *Proceedings of SPIE - The International Society for Optical Engineering*, 12232, 1223215, doi: <https://doi.org/10.1117/12.2633097>
18. Yaloveha, V., Orlova, T., Podorozhniak, A., Kuchuk, H. and Gorbulik, V. (2023), "Modern Applications of High-Resolution Multispectral EuroPlanet Dataset", *2023 IEEE 4th KhPI Week on Advanced Technology, KhPI Week 2023 - Conference Proceedings*, doi: <https://doi.org/10.1109/KhPIWeek61412.2023.10312851>
19. Cole, R.K., Fredrick, C., Nguyen, N.H. and Diddams, S.A. (2023), "Precision Doppler shift measurements with a frequency comb calibrated laser heterodyne radiometer", *Optics Letters*, vol. 48(20), pp. 5185–5188, doi: <https://doi.org/10.1364/OL.500652>
20. Kudriashov, V., Garbar, A.Y., Lukin, K.A., Maslikowski, L., Samczynski, P. and Kulpa, K. S. (2015), "Fusion of Images Generated by Radiometric and Active Noise SAR", *Cybernetics and Information Technologies*, vol. 15(7), pp. 58–66, doi: <https://doi.org/10.1515/cait-2015-0089>
21. Hashimov, E.G., Bayramov, A.A. and Sabziev, E.N. (2017), "Determination of the bearing angle of unobserved ground targets by use of seismic location cells", *ICMT 2017 - 6th International Conference on Military Technologies*, pp. 185–188, 7988753, doi: <https://doi.org/10.1109/MILTECHS.2017.7988753>
22. Ibrahimov, B., Hashimov, E. and Ismayilov, T. (2024), "Research and analysis mathematical model of the demodulator for assessing the indicators noise immunity telecommunication systems", *Advanced Information Systems*, vol. 8, no. 4, pp. 20–25, doi: <https://doi.org/10.20998/2522-9052.2024.4.03>
23. Lukin, K. A. and Kudriashov, V. V. (2013), "Fusion of synthetic aperture radiometer and noise waveform SAR images", *2013 IX International Conference on Antenna Theory and Techniques*, pp. 549–551, doi: <https://doi.org/10.1109/ICATT.2013.6650843>
24. Ruban, I., Kuchuk, H., Kovalenko, A., Lukova-Chuiko, N. and Martovytsky, V. (2021), "Method for Determining the Structural Reliability of a Network Based on a Hyperconverged Architecture", *Studies in Computational Intelligence*, vol. 976, pp. 147–163, doi: [https://doi.org/10.1007/978-3-030-74556-1\\_9](https://doi.org/10.1007/978-3-030-74556-1_9)
25. Kudriashov, V., Martin-Neira, M., Roelofs, F., Falcke, H., Brinkerink, C., Baryshev, A., Hogerheijde, M., Young, A., Pourshaghghi, H., Klein-Wolt, M., Moscibrodzka, M., Davelaar, J., Barat, I., Duesmann, B., Valenta, V., Perdignes Armengol, J.M., De Wilde, D., Martin Iglesias, P., Alagha, N., Van Der Vorst, M. (2021), "An Event Horizon Imager (EHI) Mission Concept Utilizing Medium Earth Orbit Sub-mm Interferometry", *Chinese Journal of Space Science*, vol. 41(2), pp. 211–233, doi: <https://doi.org/10.11728/cjss2021.02.211>
26. Bayramov, A.A., Hashimov, E.G. and Nasibov, Y.A. (2020), "Unmanned aerial vehicle applications for military GIS task solutions", *Research Anthology on Reliability and Safety in Aviation Systems, Spacecraft, and Air Transport*, pp. 1092–1115, doi: <https://doi.org/10.4018/978-1-7998-5357-2.ch044>

27. Unal, B., Bagcier, S., Simsir, I., Bilgili, Y. and Kara, S. (2004), "Evaluation of differences between observers and automatic-manual measurements in calculation of Doppler parameters", *Journal of Ultrasound in Medicine*, vol. 23(8), pp. 1041–1048, doi: <https://doi.org/10.7863/jum.2004.23.8.1041>
28. Kuchuk, H. and Kuliakin, A. (2024), "Hybrid Recommender For Virtual Art Compositions With Video Sentiments Analysis", *Advanced Information Systems*, vol. 8, no. 1, pp. 70–79, doi: <https://doi.org/10.20998/2522-9052.2024.1.09>
29. Al-Amri, M.F.A. and Al-Shammari, B.K.J. (2024), "An overview of Doppler effect deviation in high mobility communication systems", *AIP Conference Proceedings*, vol. 3232(1), 020002, doi: <https://doi.org/10.1063/5.0238108>
30. Pavlikov, V.V., Odokiyenko, A.V. and Sobkolov, A.D. (2017), "Comparison of dicke and ratio type modulation radiometers statistical characteristics of signal parameter estimates and fluctuation sensitivities", *MRRS 2017 - 2017 IEEE Microwaves, Radar and Remote Sensing Symposium*, Proceedings, pp. 31–36, 8075019, doi: <https://doi.org/10.1109/MRRS.2017.8075019>

Received (Надійшла) 13.10.2024

Accepted for publication (Прийнята до друку) 29.01.2025

ABOUT THE AUTHORS / ВІДОМОСТІ ПРО АВТОРІВ

- Кудряшов Віктор Євгенович** – кандидат технічних наук, СНС, старший науковий співробітник відділу нелінійної динаміки електронних систем, Інститут радіофізики та електроніки ім. О.Я. Усикова НАН України, Харків, Україна;  
**Viktor Kudriashov** – Candidate of Technical Sciences, Senior Researcher, Senior Researcher of the Department of Nonlinear Dynamics of Electronic Systems, O.Ya. Usikov Institute for Radiophysics and Electronics of the NAS of Ukraine, Kharkiv, Ukraine; e-mail: [Viktor\\_Kudriashov@gmail.com](mailto:Viktor_Kudriashov@gmail.com); ORCID Author ID: <https://orcid.org/0000-0002-7055-5357>; Scopus Author ID: <https://www.scopus.com/authid/detail.uri?authorId=36478648000>.
- Коломійцев Олексій Володимирович** – доктор технічних наук, професор, професор кафедри комп'ютерної інженерії та програмування Національного технічного університету «Харківський політехнічний інститут», Харків, Україна;  
**Oleksii Kolomiitsev** – Doctor of Technical Sciences, Professor, Professor of Computer Engineering and Programming Department, National Technical University «Kharkiv Polytechnic Institute», Kharkiv, Ukraine; e-mail: [alexis\\_k@ukr.net](mailto:alexis_k@ukr.net); ORCID ID: <https://orcid.org/0000-0001-8228-8404>; Scopus ID: <https://www.scopus.com/authid/detail.uri?authorId=57211278112>.
- Лукін Костянтин Олександрович** – доктор фізико-математичних наук, професор, завідувач відділу нелінійної динаміки електронних систем, Інститут радіофізики та електроніки ім. О.Я. Усикова НАН України, Харків, Україна;  
**Kostyantyn Lukin** – Doctor of Physical and Mathematical Sciences, Professor, Head of the Department of Nonlinear Dynamics of Electronic Systems, O.Ya. Usikov Institute for Radiophysics and Electronics of the NAS of Ukraine, Kharkiv, Ukraine; e-mail: [Kostyantyn\\_Lukin@gmail.com](mailto:Kostyantyn_Lukin@gmail.com); ORCID Author ID: <https://orcid.org/0000-0001-9998-9207>; Scopus Author ID: <https://www.scopus.com/authid/detail.uri?authorId=16402414700>.
- Сліпченко Микола Іванович** – доктор фізико-математичних наук, професор, професор кафедри мікроелектроніки, електронних приладів та пристроїв, Національний технічний університет «ХПІ», Харків, Україна;  
**Mykola Slipchenko** – Doctor of Physics and Mathematics Sciences, Professor, Professor of the Department of Microelectronics, Electronic Devices and Devices, National Technical University «Kharkiv Polytechnic Institute», Kharkiv, Ukraine; e-mail: [naukovets.big@gmail.com](mailto:naukovets.big@gmail.com); ORCID Author ID: <https://orcid.org/0000-0002-3037-8763>; Scopus Author ID: <https://www.scopus.com/authid/detail.uri?authorId=24315146500>.
- Бернат Павел** – доктор філософії, старший викладач кафедри досліджень авіаційної безпеки Інституту льотної безпеки Університету Повітряних Сил Республіки Польща, Демблін, Польща;  
**Pawel Bernat** – PhD, Senior Lecturer of Aviation Security Studies Department of Faculty of Aviation Safety of the Polish Air Force University (Lotnicza Akademia Wojskowa), Dęblin, Poland; e-mail: [pawel.bernac@gmail.com](mailto:pawel.bernac@gmail.com); ORCID Author ID: <https://orcid.org/0000-0002-8150-9794>; Scopus Author ID: <https://www.scopus.com/authid/detail.uri?authorId=57208438568>.

**Методика числового моделювання визначення параметрів радіометричного зображення дистанційного зондування земних поверхонь бістатичним радіометром**

В. Є. Кудряшов, О. В. Коломійцев, К. О. Лукін, М. І. Сліпченко, П. Бернат

**Анотація.** В роботі представлено методику числового моделювання визначення параметрів радіометричних зображень при дистанційному зондуванні земних поверхонь бортовим бістатичним радіометром (БР). Запропоновано у якості корисних коливань використовувати мало контрастний сигнал трава-бетон та у якості носія БР – пасажирський літак АН-14 "Бджілка". Обрано для роботи БР 3-х міліметровий діапазон дожин хвиль зі смугою 22 ГГц. Проведено аналіз за шістьма можливими варіантами побудови системи картографування. Обчислені дальності дії систем, значення смуг зображення, різницевих доплерівських поправок частот об'єктів з врахуванням технічних характеристик БР та впливу атмосфери. Представлені характеристики радіометричних зображень при ймовірності вірного виявлення 0,5. Надані параметри зображень при вимірюванні різниць ходу та різницевої доплерівської поправки частоти об'єктів картографування. Розраховані на зображеннях кількість пікселів (різниць ходу) у рядку зображення, розрізнявальна здатність удовж шляху прольоту носія, поперек шляху та за різницевою доплерівською поправкою частоти. Знайдена кількість доплерівських фільтрів для кожної різниці ходу, середньоквадратичні відхилення (СКВ) похибок вимірювання різниці ходу та СКВ похибок вимірювання різницевої доплерівської поправки частоти об'єктів. Проведені розрахунки значень флуктуаційної чутливості БР за варіантами побудови. Представлені аналітичні вирази методики числового моделювання для проведення розрахунків та отриманий відповідний графічний матеріал.

**Ключові слова:** методика числового моделювання; радіометричне зображення; дистанційне зондування; бістатичний радіометр; дальність дії; смуга зображення; доплерівська поправка частоти; розрізнявальна здатність.